Journal of Materials Chemistry A

Accepted Manuscript

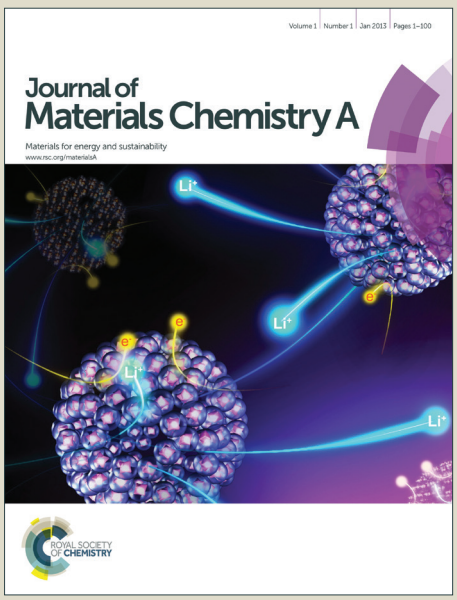

ROYAL SOCIETY OF CHEMISTRY

www.rsc.org/materialsA

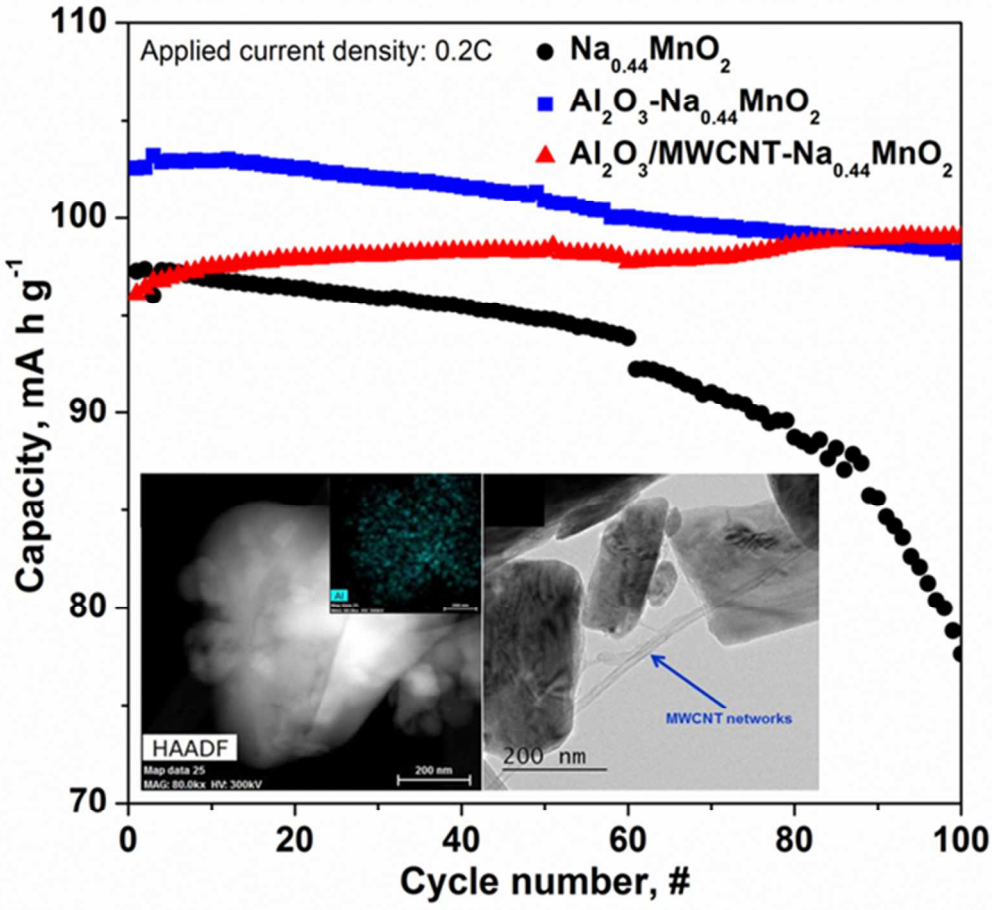

The bonding nature of Na0.44MnO2 particle surfaces is tailored by introducing Al2O3 nanopowder and/or multiwalled carbon nanotubes (MWCNTs).
109x100mm (150 x 150 DPI)

Journal of
Materials Chemistry A

RSCPublishing

Paper

Improving Kinetics and Surface Stability of Sodium Manganese Oxide Cathode Materials for Sodium Rechargeable Batteries with Al_2O_3/MWCNT Hybrid Networks

Cite this: DOI: 10.1039/x0xx00000x

Received ooth January 2012,
Accepted ooth January 2012

DOI: 10.1039/x0xx00000x

www.rsc.org/

Jun-Ho Park,[a] Kwang-Jin Park,[a] Ryoung-Hee Kim,[a] Dong-Jin Yun,[b] Seong-Yong Park,[b] Dong-Wook Han,[*a] Seok-Soo Lee,[a] and Jin-Hwan Park[a]

We report the design and fabrication of a novel functional material in which protective Al_2O_3 nanoparticles are merged with highly conductive multiwalled carbon nanotubes (MWCNTs). In this paper, we discuss in detail the effects of the Al_2O_3/MWCNT hybrid networks on the electrochemical performance of sodium manganese oxide ($Na_{0.44}MnO_2$), which is used as an electrode material in sodium rechargeable batteries. The Al_2O_3/MWCNT hybrid networks, which are uniformly dispersed on the surface of $Na_{0.44}MnO_2$, change its surface bonding nature, resulting in the improvement of the cycling performance and rate-capability of $Na_{0.44}MnO_2$. We ascribe these enhancements in performance to the inhibition of the formation of damaging NaF-based solid-electrolyte interface (SEI) layers during cycling, which enables facile transfer of Na ions through the $Na_{0.44}MnO_2$ electrode/electrolyte interfaces. Our findings regarding the control of the chemistry and bonding structure of the $Na_{0.44}MnO_2$ particle surfaces induced by the introduction of the Al_2O_3/MWCNT functional hybrid networks provide insight into the possibilities for achieving sodium rechargeable batteries with high power density and stability.

Introduction

Widespread and increasing interest in the storage of renewable energy derived from the sun, wind, and water have spurred the development of energy storage systems made from eco-friendly, abundant, and low-cost elements. Lithium rechargeable batteries have been accepted as one of the most representative energy storage and/or powering systems; however, the gradual exhaustion of natural lithium resources followed by rapid cost increase may not guarantee their consistent use in future.[1-6] Thus, nonlithium rechargeable batteries with low cost and excellent cycle life should be developed for preparing potential lithium crisis.[7,8]

Sodium rechargeable batteries have emerged as promising replacement energy storage systems for lithium rechargeable batteries because sodium is abundant and environmentally benign.[9] In particular, similarities in the redox potential ($E^0_{(Na+/Na)}$ and $E^0_{(Li+/Li)}$ are -2.71 and -3.04 V vs. S.H.E., respectively) and insertion mechanism of sodium and lithium-based chemistries have led to a rapid development in cathode materials for sodium rechargeable batteries, including sodium transition metal oxides,[10-15] phosphates,[16-20] and fluorophosphates.[21,22] However, the precise reaction mechanism operating in the sodium ion battery cathode materials has not been fully understood yet because of the lack of an appropriate electrolyte, in addition to the unwanted decomposition of electrolyte solutions on the surfaces of cathode particles. Hence, one of the most important challenges in sodium-based battery technologies is to suppress the negative effects of electrolyte decomposition on the surface properties of cathode materials.[23]

Tailoring the bonding nature of the electroactive particle surfaces toward Li ion insertion/extraction has been accomplished mainly by surface modification with carbonaceous or inactive oxide materials.[24-30] The surface tailoring has improved the chemical and electrochemical stabilities of electrode material surfaces, which has advanced the commercialization of lithium rechargeable batteries. Likewise, the surface structure of the cathode materials used in sodium rechargeable batteries needs modification depending on the physical properties of the potential functioning materials and the chemical bonds that newly form on the surface of the active materials. Surprisingly, however, there seems to be a dearth of in-depth studies verifying the effects of surface reformations on the mechanism of Na ion reactions on the surface of the cathode materials, which prevents the practical application of cathode materials in sodium rechargeable batteries.

In this paper, we describe the use of sodium manganese oxides ($Na_{0.44}MnO_2$) with surface structures modified by Al_2O_3/MWCNT hybrid networks as a cathode material for sodium rechargeable batteries. Orthorhombic $Na_{0.44}MnO_2$ exhibits excellent structural stability owing to the presence of tunnel-type crystal structure, which reduces the stress/strain occurring when Na ions are inserted in to or extracted from $Na_{0.44}MnO_2$.[31-34] This feature convinced us that most of the effects resulting from variations in the $Na_{0.44}MnO_2$ bulk crystallography could be excluded and we could focus on the surface properties. In general, Al_2O_3 has been widely adopted as a functional material capable of stabilizing the interface between active materials and the electrolyte.[35-38] However, when the surfaces of the active particles are covered by inert Al_2O_3, the kinetics of the Al_2O_3-assisted active materials could deteriorate primarily because of the low electronic conductivity of Al_2O_3.[39,40] Thus, we designed a novel functional material in which highly protective Al_2O_3 was merged with highly conductive multiwalled carbon nanotubes (MWCNTs) with a large surface area.[29] Al_2O_3 and MWCNTs were uniformly interconnected on the surfaces of the $Na_{0.44}MnO_2$ particles through high energy dispersive mechanochemical reactions. To the best of our knowledge, this is the first paper to report a distinctive hybrid surface tailoring method, which demonstrates positive effects on the electrochemical performance of transition metal oxide cathode materials.

The aim of the present study is to elucidate the effects of Al_2O_3/MWCNT hybrid surface networks on the surface structure and electrochemical performance of $Na_{0.44}MnO_2$ cathode materials for sodium rechargeable batteries.

Experimental

Synthesis and physicochemical characterization

$Na_{0.44}MnO_2$ was prepared by a conventional solid state reaction using Na_2CO_3 (Aldrich, 99.5%) and Mn_2O_3 (Aldrich, 99%) as starting materials. After mixing stoichiometric amounts of the reactants using a paste mixer (1000 rpm, 10 min.), the obtained precursor mixture was crystallized at 900 ℃ for 10 h in air flow. The surface-modified $Na_{0.44}MnO_2$ was prepared by using a Nobilta mechano-fusion system (Hosokawa Micron Corporation). Al_2O_3 nanopowder (Aldrich, 99.0%, ≤10 nm) and/or MWCNTs (Hanwha) were adopted as functional materials for tailoring the structure of the surface bonds on $Na_{0.44}MnO_2$. X-ray diffraction (XRD) patterns of pristine and surface-modified $Na_{0.44}MnO_2$ were acquired using a Bruker AXS D8 Advance X-ray diffractometer (Cu Kα radiation, λ = 1.5406 Å) to identify the different phases present. The morphology of the products was observed by scanning electron microscopy (SEM, Hitachi, S-5500) and high-resolution transmission electron microscopy (HRTEM, FEI, TITAN-80-300). The actual Na/Mn and Al/Mn ratios of the final materials as well as the amount of dissolved Mn into the electrolyte after cycling were verified by inductively coupled plasma atomic emission spectroscopy (ICP-AES, Shimadzu, ICPS-8100). Further, X-ray photoelectron spectroscopy (XPS, Ulvac PHI, VersaProbe) was carried out to acquire the Al 2p, Mn 2p, C 1s, F 1s, and O 1s core binding energies from the samples. The BET surface areas and carbon contents of the products were estimated using a surface area analyzer (BET, BEL Japan Inc., BELSORP-max) and element analyzer (EA, Thermo Scientific, FLASH 2000 series), respectively. The electronic conductivities of the powders were measured by a four-point probe powder resistivity measurement system (Mitsubishi chemical Hiresta-up).

Electrochemical characterization

Electrodes were fabricated from a mixture containing 80 wt% of the active material and 10 wt% of Denka black, which was added to a solution of N-methyl-2-pyrrolidene (NMP) containing 10 wt% polyvinylidene fluoride (PVDF). The resulting slurry was pasted onto an Al foil current collector and dried at 120 ℃ for 2 h in a vacuum oven. After pressing, the dried paste was punched into a disc (of 1.2 cm in diameter). The electrochemical properties of the fabricated electrodes were evaluated by constructing 2032 coin-type cells assembled in an Ar-filled glove box. Na was used as the counter electrode and 1M $NaPF_6$ dissolved in propylene carbonate (PC) was used as the electrolyte.

The charge/discharge characteristics of the assembled cells were examined at 25 ℃ using a battery cycler (Toscat-3100, Toyo System). The cells were charged and discharged galvanostatically in the potential range 2.0–3.8 V (vs. Na^+/Na) with a variety of current densities ranging from 0.1 to 20 C-rate. Cyclic voltammetry (CV) measurements were carried out between 2.0 and 3.8 V (vs. Na^+/Na) at a scan rate of 0.1 mV s^{-1}. To identify the kinetics of the pristine and surface-modified $Na_{0.44}MnO_2$, the activated two-electrode cells (Working: $Na_{0.44}MnO_2$, counter and reference: Na) were subjected to electrochemical impedance spectroscopy (EIS) after cell formation and 100 cycles, with a sinusoidal voltage signal (10 mV) over a frequency ranging from 100 kHz to 100 mHz. The electrodes were washed with dimethyl carbonate (DMC) to remove residual Na salts from the electrolyte before carrying out ex situ XRD and XPS analyses.

Results and discussion

Fig. 1a to 1d shows the scanning electron microscopy (SEM) images of the pristine and surface-modified $Na_{0.44}MnO_2$. We denote the surface-modified ones that were combined with a small amount of aluminum oxide (Al_2O_3) nanoparticles and Al_2O_3/MWCNT on their surfaces as Al_2O_3-$Na_{0.44}MnO_2$ and Al_2O_3/MWCNT-$Na_{0.44}MnO_2$, respectively. Pristine $Na_{0.44}MnO_2$ consisted of rectangular primary particles with an average width of less than 5 μm (Fig. 1a). However, no significant changes were found in the overall morphology of $Na_{0.44}MnO_2$ particles when comparing the pristine $Na_{0.44}MnO_2$ and Al_2O_3-$Na_{0.44}MnO_2$ samples (Fig. 1b). However, the presence of Al_2O_3 on the surfaces of Al_2O_3-$Na_{0.44}MnO_2$ particles was identified by energy dispersive X-ray spectroscopy (EDS) analysis, as marked in Fig. 1c. The incorporated MWCNTs, which blended with Al_2O_3 and $Na_{0.44}MnO_2$ particles, adhered to the surfaces of $Na_{0.44}MnO_2$ particles and the surface morphology of the Al_2O_3/MWCNT-$Na_{0.44}MnO_2$ particles seemed deformed (Fig. 1d). Further morphological analysis of the particle was carried out by HRTEM. Fig. 1e and 1f exhibit the HRTEM micrographs of pristine $Na_{0.44}MnO_2$ and Al_2O_3-$Na_{0.44}MnO_2$, along with the corresponding selected area electron diffraction (SAED) patterns. SAED patterns of both pristine $Na_{0.44}MnO_2$ and Al_2O_3-$Na_{0.44}MnO_2$ indicate the presence of crystalline $Na_{0.44}MnO_2$ particles. The distorted lattice fringes formed on the outermost Al_2O_3-$Na_{0.44}MnO_2$ particles could be associated with thin Al_2O_3 atomic layers. The uniform distribution of Al on the whole surface of $Na_{0.44}MnO_2$ particles was confirmed by EDS mapping (Fig. 1g). In addition, we found that the

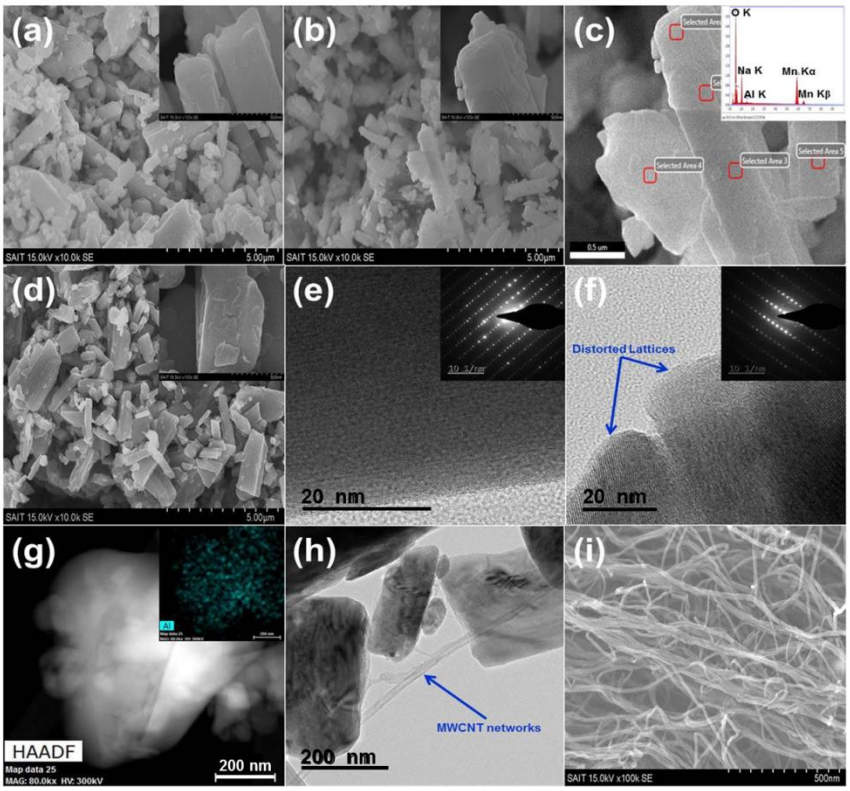

Fig. 1 (a) Scanning electron microscopy (SEM) images of (a) pristine, (b) Al_2O_3-, and (d) Al_2O_3/MWCNT-$Na_{0.44}MnO_2$. (c) Energy dispersive X-ray spectrum of Al_2O_3-$Na_{0.44}MnO_2$. High resolution transmission electron microscopy (HRTEM) images and selected area electron diffraction (SAED) patterns of (e) pristine and (f) Al_2O_3-$Na_{0.44}MnO_2$. (g) Scanning transmission electron microscope (STEM) images and EDS mapping (Al) of Al_2O_3-$Na_{0.44}MnO_2$. (h) TEM image of Al_2O_3/MWCNT-$Na_{0.44}MnO_2$. (i) SEM image of MWCNTs.

MWCNT networks (Fig. 1i) connected neighboring $Na_{0.44}MnO_2$ particles in Al_2O_3/MWCNT-$Na_{0.44}MnO_2$.

The crystal structures of pristine $Na_{0.44}MnO_2$ and surface-modified $Na_{0.44}MnO_2$ were verified by XRD (Fig. S1†). The XRD pattern acquired from pristine $Na_{0.44}MnO_2$ coincides with the Inorganic Crystal Structure Database (ICSD) reference pattern corresponding to tunnel-type $Na_{0.44}MnO_2$ (ICSD-261314) with orthorhombic crystal structure, confirming the absence of any secondary phases. In addition, no notable changes in the XRD peak positions and peak ratios were observed in the Al_2O_3 nanopowder and Al_2O_3/MWCNT-$Na_{0.44}MnO_2$ in comparison to pristine $Na_{0.44}MnO_2$, indicating that the crystal structure of $Na_{0.44}MnO_2$ was retained even after high energy dispersive mechanochemical reactions with Al_2O_3 or MWCNTs. The absence of specific peaks corresponding to Al_2O_3 and MWCNTs in the XRD patterns of the surface-modified $Na_{0.44}MnO_2$ could be attributed to the lack of Al_2O_3 (0.5 wt%) and MWCNT (1 wt%) in sufficient concentrations and the amorphous nature of Al_2O_3 and the MWCNTs. The actual Na/Mn and Al/Mn ratios of the materials measured by ICP–AES are provided in Table S1 (supporting information).

The results of the XPS analyses of pristine and surface-modified $Na_{0.44}MnO_2$ particles are shown in Fig. 2. We confirmed from the Al 2p XPS core peaks (Fig. 2a) that the incorporated Al_2O_3 nanopowder particles were located on the surface of the Al_2O_3 and Al_2O_3/MWCNT-$Na_{0.44}MnO_2$ particles, which is consistent with the EDS results presented in Fig. 1c and 1g. In addition, we compared the C 1s XPS core peaks from pristine and surface-modified $Na_{0.44}MnO_2$, which proved the presence of MWCNTs in the Al_2O_3/MWCNT-$Na_{0.44}MnO_2$ sample.[41] This agrees well with the observation of MWCNT networks in the case of the Al_2O_3/MWCNT-$Na_{0.44}MnO_2$ samples in the SEM (Fig. 1h). Meanwhile, the oxidation states of central Mn ions in $Na_{0.44}MnO_2$ were estimated from the Mn 2p XPS core peaks, accompanied by their peak deconvolution, as presented in Fig. 2c. No variation was observed in the oxidation states (Mn^{3+}/Mn^{4+} ratio = ca. 0.16) of Mn ions between the pristine $Na_{0.44}MnO_2$ and Al_2O_3-$Na_{0.44}MnO_2$ particles; however, the Mn^{3+}/Mn^{4+} ratio in $Na_{0.44}MnO_2$ increased to around 0.69 when the $Na_{0.44}MnO_2$ particles were uniformly mixed with MWCNTs. We assume that the partial oxidation of MWCNTs during the high energy dispersive mechanochemical reaction possibly contributes to the reduction of Mn ions near the surfaces of the $Na_{0.44}MnO_2$ particles. These findings were also supported by the O 1s XPS core peaks originating from pristine and surface-modified $Na_{0.44}MnO_2$; the intensity of the characteristic peak (observed at around 529.8 eV) for MnO_2 was highly diminished in the case of Al_2O_3/MWCNT-$Na_{0.44}MnO_2$, which was significantly different from $Na_{0.44}MnO_2$ without MWCNTs.

The initial insertion/extraction reactions of Na ions into/out of the pristine $Na_{0.44}MnO_2$ and surface-modified $Na_{0.44}MnO_2$ after cell fabrication were investigated by CV (profiles are shown in Fig. 3a). At least six pairs of reversible reactions were observed for all the materials although the correlation between the variation in the crystal structure and the consecutive two-phase transitions is yet to be completely understood.[42,43] The difference in the peak voltage between a pair of anodic and cathodic reactions for $Na_{0.44}MnO_2$ observed at less than 2.8 V vs. Na^+/Na was remarkably diminished by Al_2O_3 and

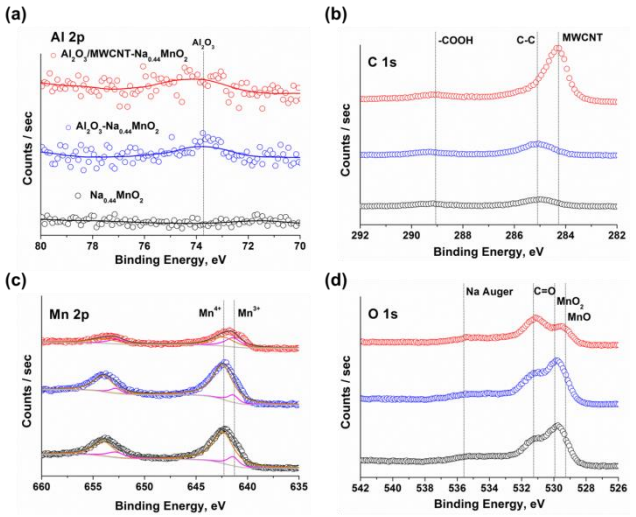

Fig. 2 (a) Al 2p, (b) C 1s, (c) Mn 2p, and (d) O 1s XPS core peaks acquired from pristine and surface-modified $Na_{0.44}MnO_2$ before cycling.

Al_2O_3/MWCNT incorporation. The CV profiles of the pristine and surface-modified $Na_{0.44}MnO_2$ are in good agreement with their galvanostatic (rate 0.1 C) voltage profiles in the range 2.0–3.8 V (vs. Na^+/Na), as described in Fig. 3b. The reversible charge-discharge curves of the prepared samples agree well with previous reports on the charge-discharge behavior of $Na_{0.44}MnO_2$.[42,43] The lower discharge capacity (100.2 mA h g^{-1}) of pristine $Na_{0.44}MnO_2$ in comparison to Al_2O_3-$Na_{0.44}MnO_2$ (105.3 mA h g^{-1}) can be attributed to the modification in the surface properties of the $Na_{0.44}MnO_2$ particles induced by the presence of Al_2O_3. In contrast, the discharge capacity of Al_2O_3/MWCNT-$Na_{0.44}MnO_2$ was almost identical to that of pristine $Na_{0.44}MnO_2$ because a part of the reactive area formed on the surface of the $Na_{0.44}MnO_2$ particles in the initial state could be deactivated by the surrounding MWCNT networks with a large surface area (Table S1).

We evaluated the rate-capabilities of the pristine $Na_{0.44}MnO_2$ and surface-modified $Na_{0.44}MnO_2$ at a variety of current densities ranging from 0.1 to 20 C (the results are presented in Fig. 3c). At low current densities (rates ≤ 0.5 C), the extent of the discharge capacity degradation of $Na_{0.44}MnO_2$ is not a function of Al_2O_3 and MWCNT incorporation. In contrast, the extent of capacity loss at a high current density (≥1 C) is highly suppressed by Al_2O_3 and Al_2O_3/MWCNT incorporation, which is indicative of facile Na ion insertion/extraction into/out of the $Na_{0.44}MnO_2$ particles. This is in agreement with the CV results, which show a reduction in the peak voltage between a pair of anodic and cathodic reactions (Fig. 3a). One of the most important points here is the similarity of the rate-capabilities of Al_2O_3-$Na_{0.44}MnO_2$ and Al_2O_3/MWCNT-$Na_{0.44}MnO_2$, which proves that the ionic conduction of sodium ions through $Na_{0.44}MnO_2$ the electrode/electrolyte interfaces is a more crucial factor than the electronic conduction in the determination of the kinetic properties of $Na_{0.44}MnO_2$. Compared to pristine and Al_2O_3-$Na_{0.44}MnO_2$, the electrical conductivity of Al_2O_3/MWCNT-$Na_{0.44}MnO_2$ was approximately three orders of magnitude higher because of the addition of conductive MWCNTs, was shown in Fig S2†. These findings are special as they counterintuitive in terms of the expected the rate performance of transition metal oxides with poor electronic conductivity.

The cycling performances (rate 0.2 C) of pristine $Na_{0.44}MnO_2$ and surface-modified $Na_{0.44}MnO_2$, measured in the range 2.0–3.8 V (vs. Na^+/Na) are shown in Fig. 3d. While the discharge capacity of pristine $Na_{0.44}MnO_2$ abruptly decreased after around 60 cycles, Al_2O_3-$Na_{0.44}MnO_2$ exhibited considerably high discharge capacity (of 98.2 mA h g^{-1}), corresponding to ~ 95.8 % of its initial discharge capacity even after 100 cycles. Meanwhile, Al_2O_3/MWCNT-$Na_{0.44}MnO_2$ exhibited entirely different capacity fading properties when compared with the other samples and the discharge capacity of Al_2O_3/MWCNT-$Na_{0.44}MnO_2$ continued to increase from ~ 96.1 mA h g^{-1} to ~ 99.0 mA h g^{-1} during 100 cycles. Considering that the long-term cycling performance of $Na_{0.44}MnO_2$ is associated with the

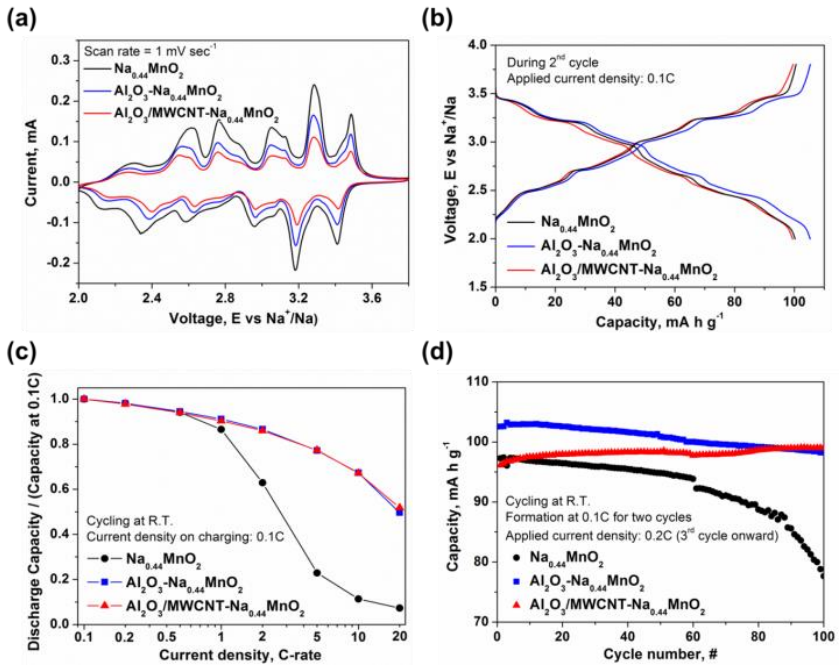

Fig. 3 (a) Cyclic voltammetry (CV) profiles, (b) galvanostatic (rate 0.1 C) voltage profiles voltage, (c) rate-capability, and (d) cycling performance (rate 0.2 C) of pristine and surface-modified $Na_{0.44}MnO_2$ in the range 2.0–3.8 V (vs. Na^+/Na).

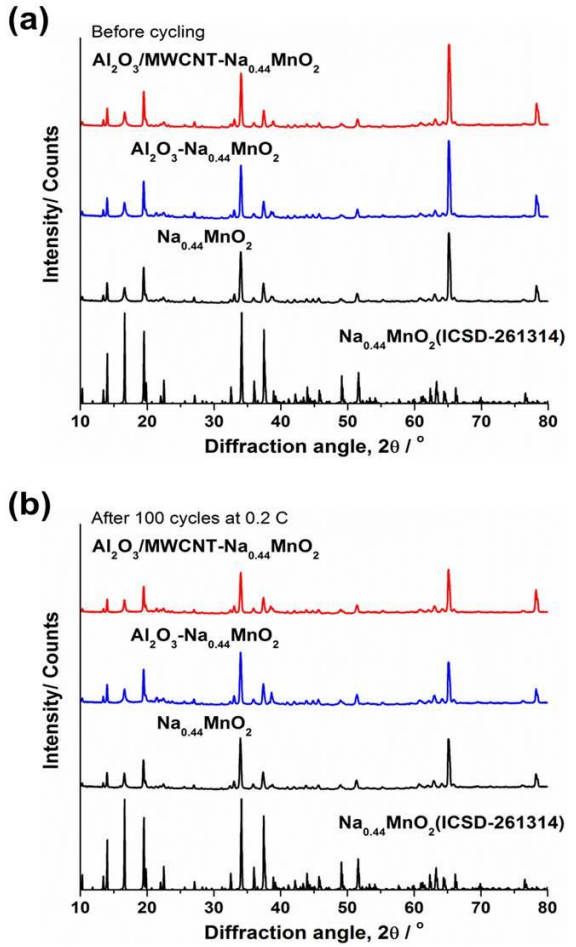

Fig. 4 Ex situ X-ray diffraction (XRD) patterns of pristine and surface-modified $Na_{0.44}MnO_2$ obtained (a) before cycling and (b) after 100 cycles (rate 0.2 C).

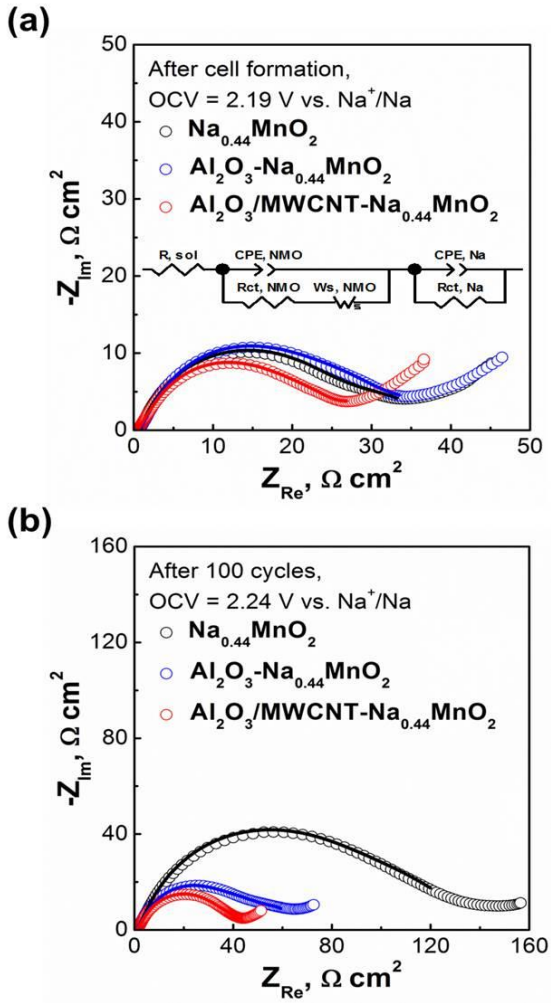

Fig. 5 Electrochemical impedance spectroscopy (EIS) spectra and equivalent circuit model of pristine and surface-modified $Na_{0.44}MnO_2$ measured (a) after cell formation and (b) after 100 cycles (rate 0.2 C).

structural and/or chemical stabilities of $Na_{0.44}MnO_2$ particles not only in the bulk crystal structure but also on the surface,[35,44] the origin of improvements in the cycling performance of $Na_{0.44}MnO_2$ assisted by a small amount of Al_2O_3 and Al_2O_3/MWCNTs should be considered separately in the light of the bulk and surface properties of the $Na_{0.44}MnO_2$ particles.

We performed ex situ XRD analyses on the pristine and surface-modified $Na_{0.44}MnO_2$ electrodes to investigate the crystallographic changes occurring in the bulk during cycling, and the results measured before cycling and after 100 cycles (0.2 C-rate, galvanostatic) are shown in Fig. 4. We found that the pristine $Na_{0.44}MnO_2$ electrode exhibited XRD patterns comparable to the Al_2O_3 and Al_2O_3/MWCNT-$Na_{0.44}MnO_2$ electrodes before cycling. In addition, all the three XRD patterns tended to change in a similar manner during cycling, together with a substantial reduction in the intensities of the overall peaks. This result was also supported by the ICP-AES analyses used for measuring the amount of dissolved Mn into the electrolyte after cycling. Negligible amount of Mn (< 1ppm, which could not be measured) was detected in all the samples. Thus, it could be simply concluded that the discrepancy in the cycling performance between pristine and surface-modified $Na_{0.44}MnO_2$ was not a function of the structural stability of the $Na_{0.44}MnO_2$ bulk crystals.

The electrochemical reactions and their kinetics were identified for pristine $Na_{0.44}MnO_2$ and surface-modified $Na_{0.44}MnO_2$ after cell formation and after 100 cycles by EIS, as shown in Fig. 5. The EIS analysis is one of the most appropriate tools for demonstrating different kinds of resistances linked to charge transfer at the electrode/electrolyte interface or inside the electrode. The established equivalent circuit model is also included in Fig. 5a. The charge transfer resistance ($R_{ct,NMO}$) at the cathode sides of the pristine $Na_{0.44}MnO_2$, Al_2O_3-$Na_{0.44}MnO_2$, and Al_2O_3/MWCNT-$Na_{0.44}MnO_2$ were 23.6, 24.9, and 19.5 Ω cm^2, respectively, after cell formation. The significantly lower $R_{ct,NMO}$ of the Al_2O_3/MWCNT-$Na_{0.44}MnO_2$ compared to that shown by the other samples might be associated with its much higher electrical conductivity (Fig S2†), which is induced by the presence of MWCNTs. Meanwhile, after 100 cycles, the $R_{ct,NMO}$ of the pristine $Na_{0.44}MnO_2$ sample increased from 23.6 to 56.8 Ω cm^2 but the extent of increase in $R_{ct,NMO}$ was definitely reduced in the case of surface-modified $Na_{0.44}MnO_2$. In particular, the Al_2O_3/MWCNT-$Na_{0.44}MnO_2$ sample featured a much lower value of $R_{ct,NMO}$ (25.8 Ω cm^2) than the pristine sample. From these results, we conjecture that the improved cycling performance of $Na_{0.44}MnO_2$ resulting from the surface reforming caused by Al_2O_3 and the Al_2O_3/MWCNT network resulted from the reduced charge transfer resistance at the $Na_{0.44}MnO_2$ electrode/electrolyte interfaces. These findings

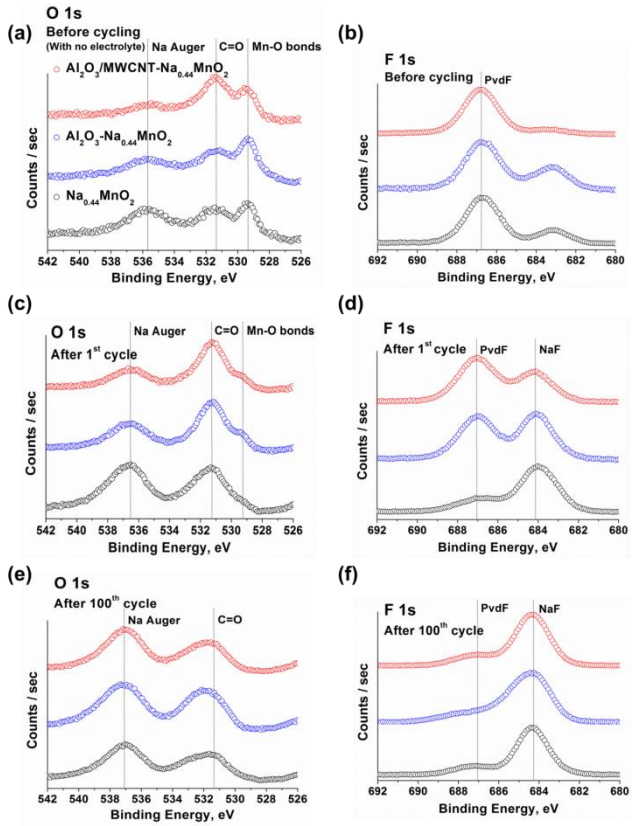

Fig. 6 O 1s and F 1s ex situ XPS core peaks acquired from pristine and surface-modified $Na_{0.44}MnO_2$ measured (a, b) before cycling, (c, d) after the 1st cycle, and (e, f) after 100 cycles (rate 0.2 C).

imply that the surface properties of the $Na_{0.44}MnO_2$ particles play a crucial role in the facile migration of Na ions migration into/out of $Na_{0.44}MnO_2$ particles.

We believe that these findings including high Li ion transport and structure stabilization induced by Zr incorporation suggests a totally brand-new strategy for achieving high-power Li rechargeable batteries using NASICON-structured cathode materials in combination with nano-architecture tailoring, thereby solving general issues in NASICON-structured phosphates applicable to electric vehicles and energy storage systems for renewable energy in the field of energy storage and conversion materials, as well as it lays a fundamental ground for tailoring lattice structure of materials for various energy devices such as capacitors, lithium rechargeable batteries, solar cells, and etc. as well as diverse semiconducting devices based on metal oxides.

To verify the origin of the increase in the charge transfer resistance at the $Na_{0.44}MnO_2$ electrode/electrolyte interfaces on cycling, we compared the bond structures formed on the surfaces of the pristine $Na_{0.44}MnO_2$ and surface-modified $Na_{0.44}MnO_2$ electrodes by ex situ XPS analyses. Fig. 6 shows the O 1s (Fig. 6a, c, and 6e) and F 1s (Fig. 6b, d, and 6f) XPS core peaks for all the materials acquired before cycling, after the 1st cycle, and after the 100th cycle. When the $Na_{0.44}MnO_2$ electrodes were not exposed to the electrolyte before cycling, three different O 1s XPS core peaks were observed at 535.5, 531.4, and 529.3 eV corresponding to the Auger electron signal of Na ions, C=O, and Mn-O bonds, respectively.[45] However, the presence of MWCNTs in the Al_2O_3/MWCNT-$Na_{0.44}MnO_2$ increased the intensity of the C=O bonds on the surface of the$Na_{0.44}MnO_2$ (Fig. 6a). After the 1st cycle, the peak signal of the Mn-O bonds weakened with a slight increase in the intensity of the Na Auger peak, but the extent of such peak variations was more marked in the case of pristine $Na_{0.44}MnO_2$ than in the case of surface-modified $Na_{0.44}MnO_2$ (Fig. 6c). This demonstrated that the solid electrolyte interface (SEI) layers primarily comprised of a Na composite and formed on $Na_{0.44}MnO_2$ electrodes during initial cell activation, which diminished the large reaction area of the Mn-O bonds exposed to the electrolyte. In addition, the Al_2O_3 nanopowder (Fig. 1c and Fig. 2a) and MWCNTs (Fig. 1h and Fig. 2b) located on the surfaces of the $Na_{0.44}MnO_2$ particles seemed to suppress the formation of the SEI layers. We point out, based on our analysis of the O 1s peaks in the XPS profiles of the materials after 100 cycles (Fig. 6e), that the bond structure on the surfaces of the $Na_{0.44}MnO_2$ electrodes tend to be dominated by growing SEI layers. We identified the composition of the SEI layers formed on the surface of $Na_{0.44}MnO_2$ electrodes by tracing the variation in the F 1s XPS core peaks with cycling. Two different peaks were found at 687.0 and 684.3 eV after the 1st cycle, which corresponded to the PVDF binder and NaF, respectively (Fig. 6d). It is noteworthy that the strong PVDF peak remained in the surface-modified $Na_{0.44}MnO_2$ electrodes, which differs from the pristine $Na_{0.44}MnO_2$ electrode in which the PVDF peak was remarkably weakened. Moreover, a minute survey revealed that the formation of NaF on the surface of $Na_{0.44}MnO_2$ was more suppressed by the presence of strong C=O bonds induced by the presence of MWCNTs and Al_2O_3-$Na_{0.44}MnO_2$ showed NaF peaks with higher intensity compared with Al_2O_3/MWCNT-$Na_{0.44}MnO_2$. However, after 100 cycles, the surfaces of all the $Na_{0.44}MnO_2$ electrodes were fully covered with NaF and simultaneously, the PVDF peaks disappeared, irrespective of the state of surface modification. Thus, NaF-based SEI layers are considered to be a major factor degrading the capacity of the $Na_{0.44}MnO_2$ electrodes during cycling. More importantly, the formation of NaF on the surface of the $Na_{0.44}MnO_2$ electrode can be suppressed by converting HF into the form of aluminum oxyfluorides[45] as well as by prohibiting any direct contact between the active materials and the electrolyte, which improves the cycling performance of $Na_{0.44}MnO_2$. However, the effects of weight ratio between Al_2O_3 and MWCNT on the electrochemical performance of $Na_{0.44}MnO_2$ are still in debate. Our findings suggest a novel way of maximizing the electrochemical properties of Na-based cathode materials by hybrid surface tailoring using a combination of a highly protective oxide (Al_2O_3) and conductive carbon (MWCNTs).

Conclusions

In summary, we succeeded in tailoring the bonding nature of $Na_{0.44}MnO_2$ particle surfaces by introducing Al_2O_3 nanopowder and/or multiwalled carbon nanotubes (MWCNTs). Surface-modified $Na_{0.44}MnO_2$ (Al_2O_3- and Al_2O_3/MWCNT-$Na_{0.44}MnO_2$) showed superior electrochemical performance when compared to pristine $Na_{0.44}MnO_2$. In particular, the discharge capacity of Al_2O_3/MWCNT-$Na_{0.44}MnO_2$ increased to 99.0 mA h g^{-1} after 100 cycles, but pristine $Na_{0.44}MnO_2$ exhibited an abrupt decline in the discharge capacity within 60 cycles. Such an improvement in the cycling performance of $Na_{0.44}MnO_2$ is attributed to the inhibited formation of unstable solid-electrolyte interface (SEI) layers during cycling that negatively affects the cycling performance of $Na_{0.44}MnO_2$, which is induced by Al_2O_3/MWCNT hybrid networks homogeneously dispersed on the surfaces of the $Na_{0.44}MnO_2$ particles. In addition, F 1s peaks obtained during ex situ X-XPS analysis were used to identify the composition of the SEI layers formed

on the surface of the $Na_{0.44}MnO_2$ electrodes as sodium fluoride (NaF). The results of our study suggest that controlling the initial chemistries and bonding structures of the surfaces of the transition metal oxides could be a crucial factor determining their long-term cycling performance. The rate-capability of $Na_{0.44}MnO_2$ was also remarkably enhanced by Al_2O_3 and Al_2O_3/MWCNT incorporation. Surprisingly, however, no notable change in their rate performance was observed despite the observation of a large difference in the electrical conductivities of Al_2O_3-$Na_{0.44}MnO_2$ and Al_2O_3/MWCNT-$Na_{0.44}MnO_2$ samples, which proved that ionic conduction of sodium ions through the$Na_{0.44}MnO_2$ electrode/electrolyte interfaces (and not the electronic conduction) acted as the rate determining step during the Na insertion/extraction reaction process.

Acknowledgements

The authors gratefully acknowledge Y. N. Ham for ICP-AES.

Notes and references

[a] *Energy Lab, Samsung Advanced Institute of Technology, Suwon, 440-600, Republic of Korea. E-mail: dongwwook.han@samsung.com*
[b] *Analytical Science Laboratory, Samsung Advanced Institute of Technology, Suwon, 440-600, Republic of Korea.*

† Electronic Supplementary Information (ESI) available: XRD, Electrical conductivity, and ICP-AES of pristine and surface-modified $Na_{0.44}MnO_2$. See DOI: 10.1039/b000000x/

1 J.-M. Tarascon and M. Armand, *Nature*, 2001, **414**, 359-367.
2 M. Armand and J.-M. Tarascon, *Nature*, 2008, **451**, 652-657.
3 C. Liu, F. Li, M. Lai-Peng and H.-M. Cheng, *Adv. Mater.*, 2010, **22**, E28-E62.
4 X.-P. Gao and H.-X. Yang, *Energy Environ. Sci.*, 2010, **3**, 174-189.
5 M. S. Whittingham, *Chem. Rev.*, 2004, **104**, 4271-4302.
6 J. B. Goodenough and Y. Kim, *Chem. Mater*., 2010, **22**, 587-603.
7 P. Saha, M. K. Datta, O. I. Manivannan, D. Almen and P. N. Kumta, *Prog. Mater. Sci.*, 2014, **66**, 1-86.
8 V. Palomares, P. Serras, P, I. Villaluenga, K. B. Hueso, J. Carretero-González and T. Rojo, *Energy Environ. Sci*., 2012, **5**, 5884-5901.
9 M. D. Slater, D. Kim, E. Lee and C. S. Johnson, *Adv. Funct. Mater*., 2013, **23**, 947-958.
10 N. Yabuuchi, M. Kajiyama, J. Iwatate, H. Nishikawa, S. Hitomi, R. Okuyama, R. Usui, Y. Yamada and S. Komaba, *Nature Mater.*, 2012, **11**, 512-517.
11 W. Wang, M. Tamaru, M. Okubo and A. Yamada, *J. Phy. Chem.*, 2013, **117**, 15545-15551.
12 R. Berthelot, C. Didier and C. Delmas, *Nature Mater.*, 2011, **10**, 74-80.
13 M. Guignard, C. Didier, J. Darriet, J, P. Bordet, E. Elkaïm and C. Delmas, *Nature Mater.*, 2013, **12**, 74-80.
14 H. Pan, Y.-S. Hu and L. Chen, *Energy Environ. Sci.*, 2013, **6**, 2338-2360.
15 V. Palomares, P. Serras, I. Villaluenga, K. B. Hueso, J. B. Carretero-González and T. Rojo, *Energy Environ. Sci*., 2012, **5**, 5884-5901.
16 Z. Jian, W. Han, X. Lu, H. Yang, Y.-S. Hu, J. Zhou, Z. Zhou, J. Li, W. Chen, D. Chen and L. Chen, *Adv. Energy Mater.*, 2013, **3**, 156-160.
17 K. Saravanan, C. W. Mason, A. Rudola, K. H. Wong and P. Balaya, *Adv. Energy Mater.*, 2013, **3**, 444-450.
18 Y. H. Jung, C. H. Lim and D. K. Kim, *J. Mater. Chem. A*, 2013, **1**, 11350-11354.
19 J. Song, M. Xu, L. Wang and J. B. Goodenough, *Chem. Commun*., 2013, **49**, 5280-5282.
20 K. T. Lee, T. N. Ramesh, F. Nan, G. Botton and L. F. Nazar, *Chem. Mater*., 2011, **23**, 3593-3600.
21 Y.-U. Park, D.-H. Seo, H.-S. Kwon, H.-S. Kim, B. Kim, J. Kim, H. Kim, I. Kim, H.-I. Yoo and K. Kang, *J. Am. Chem. Soc* , 2013, **135**, 13870-13878.
22 Q. Wang, A. Madsen, J. R. Owen and M. T. Weller, *Chem. Commun*., 2013, **49**, 2121-2123.
23 S. Komaba, C. Takei, T. Nakayama, A. Ogata and N. Yabuuchi, *Electrochem. Commun*., 2010, **12**, 355-358.
24 Z. Chen, Y. Qin, K. Amine and Y.-K. Sun, *J. Mater. Chem.*, 2010, **20**, 7606-7612.
25 H. Li and H. Zhou, *Chem. Commun*., 2012, **48**, 1201-1217.
26 L. J. Fu, H. Liu, C. Li, Y. P. Wu, E. Rahm, R. Holze and H. Q. Wu, *Solid State Sci*., 2006, **8**, 113-128.
27 H. Li, Z. Wang, L. Chen and X. Huang, *Adv. Mater.*, 2009, **21**, 4593-4607.
28 W.-K. Kim, D.-W. Han, W.-H. Ryu, S.-J. Lim and H.-S Kwon, *Electrochim. Acta*, 2012, **71**, 17-21.
29 X. Li, F. Kang, X. Bai and W. Shen, *Electrochem. Commun*., 2007, **9**, 663-666.
30 K. J. Rosina, M. Jiang, D. Zeng, E. Salager, A. S. Best and C. P. Grey, *J. Mater. Chem*., 2012, **22**, 20602-20610.
31 I. Kruk, P. Zajdel, W. V. Beek, I. Bakaimi, A. Lappas, C. Stock and M. A. Green, *J. Am. Chem. Soc.*, 2011, **133**, 13950-13956.
32 H. Kim, D. J. Kim, D.-H. Seo, M. S. Yeom, K. Kang, D. K. Kim and Y. Jung, *Chem. Mater*., 2012, **24**, 1205-1211.
33 Y. Cao, L. Xiao, W. Wang, D. Choi, Z. Nie, J. Yu, L. V. Saraf, Z. Yang and J. Liu, *Adv. Mater*., 2011, **23**, 3155-3160.
34 E. Hosono, T. Saito, J. Hoshino, M. Okubo, Y. Saito, D. Nishio-Hamane, T. Kudo and H. Zhou, *J. Power Sources*, 2012, **217**, 43-46.
35 S. T. Myung, K. Izumi, S. Komaba, Y. K. Sun, H. Yashiro and N. Kumagai, *Chem Mater*., 2005, **17**, 3695-3704.
36 X. Xiao, D. Ahn, Z. Liu, J.-H. Kim and P. Lu, *Electrochem. Commun*., 2013, **32**, 31-34.
37 Y. S. Jung, A. S. Cavanagh, L. A. Riley, S.-H. Kang, A. C. Dillon, M. D. Groner, S. M. George and S.-H. Lee, *Adv. Mater*., 2010, **22**, 2172-2176.
38 I. D. Scott, Y. S. Jung, A. S. Cavanage, Y. Yan, A. C. Dillon, S. M. George and S.-H. Lee, *Nano Lett.*, 2011, **11**, 414-418.
39 S.-K. Hu, G.-H. Cheng, M.-Y. Cheng and B.-J. Hwang, *J. Power Sources*, 2009, **188**, 564-569.
40 Y. Huang, J. Chen, F. Cheng, W. Wan, W. Liu, H. Zhou and X. Zhang, *J. Power Sources*, 2010, **195**, 8267-8274.
41 N. G. Akalework, C.-J. Pan, W.-N. Su, J. Rick, M.-C. Tsai, J.-F. Lee, J.-M. Lin, L.-D. Tsai and B.-J. Hwang, *J. Mater. Chem.*, 2012, **22**, 20977-20985.
42 F. Sauvage, L. Laffont, J.-M. Tarascon and E. Baudrin, *Inorg. Chem.*, 2007, **46**, 3289-3294.
43 X. Zhou, R. G. Guduru and P. Mohanty, *J. Mater. Chem. A*, 2013, **1**, 2757-2761.
44 J. Liu, B. Reeja-Jayan and A. Manthiram, *J. Phyc. Chem. C*, 2010, **114**, 9528-9533.

45 M. Bettge, Y. Li, B. Sankaran, N. D. Rago, T. Spila, R. T. Haasch, I. Petrov and D. P. Abraham, *J. Power Sources*, 2013, **233**, 346-357.

